Dual-beam scrolling interference pattern flow cytometry for high-throughput characterization of submicron sized particles

Supplementary Material

Carl Emil Schøier Kovsted[1,*,X], Jaco Botha[1,*], Jeppe Revall Frisvad [2], Lasse Pærgård Andersen [1], Rodolphe Marie [1], Emil Boye Kromann [3,X]

[1] *Department of Health Technology, Technical University of Denmark, Denmark*
[2] *Department of Applied Mathematics and Computer Science, Technical University of Denmark, Denmark*
[3] *Department of Green Technology, University of Southern Denmark, Denmark*
[*] *These authors contributed equally to this work*
[X] cesk@dtu.dk
[X] ebbk@igt.sdu.dk

Corresponding authors:
Carl Emil Schøier Kovsted
cesk@dtu.dk
Department of Health Technology, Technical University of Denmark
Bygning, Ørsteds Pl. 345C, 2800 Lundtofte, Denmark

Emil Boye Kromann
ebbk@igt.sdu.dk
Department of Green Technology, University of Southern Denmark
Campusvej 55, 5230 Odense M, Denmark

Supplementary materials

1. Theory

1.1 Scattering by a homogeneous sphere illuminated by a single incident monochromatic plane wave

Here, we present the theoretical framework for calculating the scattered electromagnetic field from a spherical particle illuminated by monochromatic plane waves. The analytical approach and the reference coordinate system follow the formulations of Lorenz and Mie **[1–3]**. The resulting analytical solution describes scattering from particles spanning sizes from a fraction of the incident wavelength to several wavelengths. The model relies on a series of assumptions, including the presence of a single spherical particle with a homogeneous refractive index, illumination by a monochromatic harmonic plane wave propagating along a single dimension, and a host medium with a uniform refractive index that may be either non-absorbing or absorbing **[3,4]**. We only consider scattering in the far-field region. The geometry of the simulation with a single incident monochromatic plane wave illuminating a single particle is depicted in **Supplementary Figure 1.1**. The basis vectors of the Cartesian coordinate system are given by $\{\hat{\mathbf{e}}_x, \hat{\mathbf{e}}_y, \hat{\mathbf{e}}_z\}$, and the propagation direction of the incident wave is parallel to the z-axis. The scattered electric field is observed in the direction $\hat{\mathbf{e}}_r$. The forward direction $\hat{\mathbf{e}}_z$ and scattering direction $\hat{\mathbf{e}}_r$ span the scattering plane, which is determined by the azimuthal angle (ϕ) in the xz-plane, with the scattering plane allowing evaluation of the scattered light at any polar angle (θ) within the plane.

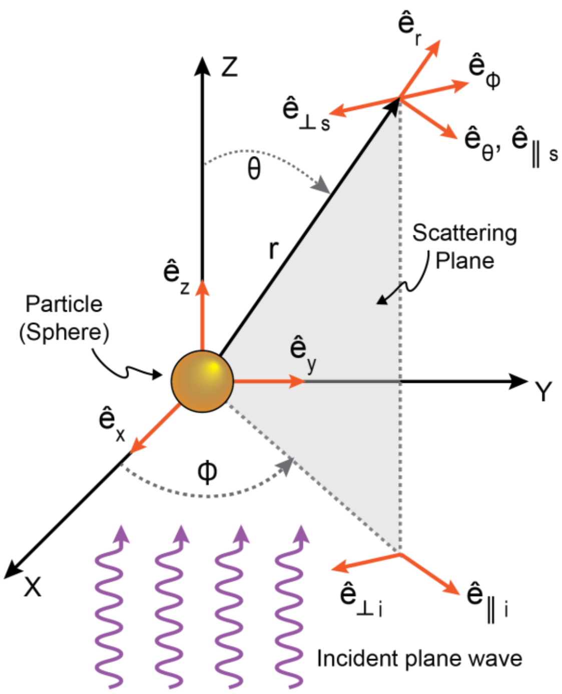

Supplementary Figure 1.1: Scattering of a monochromatic plane wave by a spherical particle. The particle is centered at the origin, with the incident electric field propagating along the z-axis. The scattering plane serves as the reference for evaluating the electric field components.

Both the incident and scattered field are resolved in a parallel (∥) or perpendicular (⊥) component of their respective plane. Based on this notation we write the incident field in orthogonal components, when considering an x-polarized monochromatic plane wave propagating along the z-axis

$$\mathbf{E}_i = (E_{0\parallel}\hat{\mathbf{e}}_{\parallel i} + E_{0\perp}\hat{\mathbf{e}}_{\perp i})e^{(ikz-i\omega t)} = E_{\parallel i}\hat{\mathbf{e}}_{\parallel i} + E_{\perp i}\hat{\mathbf{e}}_{\perp i}\,. \qquad \text{Eq. (1.1)}$$

Here, E_0 is the magnitude of the incident electric field, $e^{(ikz-i\omega t)}$ describes the oscillating nature of the electric field where $k = 2\pi\eta_{med}/\lambda$ is the wavenumber which is dependent on the refractive index of the host medium (η_{med}) and the light's wavelength (λ).

The scattered electric field is expressed as a linear function of the incident electric field and the scattering amplitude function. This relationship is written in matrix form directly showing the relationship between the polarization of the incident field and the scattered electric field as

$$\begin{pmatrix} E_{\parallel s} \\ E_{\perp s} \end{pmatrix} = \frac{e^{ik(r-z)}}{-ikr} \begin{pmatrix} S_2 & S_3 \\ S_4 & S_1 \end{pmatrix} \begin{pmatrix} E_{\parallel i} \\ E_{\perp i} \end{pmatrix}. \qquad \text{Eq. (1.2)}$$

The amplitude scattering elements S_j ($j=1,2,3,4$) are angle-dependent relative to the polar angle θ. In the case of a completely spherical particle the amplitude scattering elements S_j ($j=3,4$) are both zero, thereby reducing the expression to include only two elements. Based on this the scattered electric field and its polarizations are expressed as

$$\begin{pmatrix} E_{\parallel s} \\ E_{\perp s} \end{pmatrix} = \frac{e^{ik(r-z)}}{-ikr} \begin{pmatrix} S_2 & 0 \\ 0 & S_1 \end{pmatrix} \begin{pmatrix} E_{\parallel i} \\ E_{\perp i} \end{pmatrix}, \qquad \text{Eq. (1.3)}$$

$$E_{\parallel s} = \frac{e^{ik(rz)}}{-ikr} S_2 \cdot E_{\parallel i},$$

$$E_{\perp s} = \frac{e^{ik(r-z)}}{-ikr} S_1 \cdot E_{\perp i}.$$

The individual scattering amplitude elements are evaluated as an angle-dependent finite series **[1–3]**

$$S_1(\theta) = \sum_{n=1}^{\infty} \frac{2n+1}{n(n+1)} \big(a_n \pi_n(\cos(\theta)) + b_n \tau_n(\cos(\theta))\big), \qquad \text{Eq. (1.4)}$$

$$S_2(\theta) = \sum_{n=1}^{\infty} \frac{2n+1}{n(n+1)} \big(b_n \pi_n(\cos(\theta)) + a_n \tau_n(\cos(\theta))\big).$$

The two angle-dependent functions π_n and τ_n are related to the Legendre polynomials (P_n) and are evaluated as upwards recurrences, given that $\mu = cos(\theta)$ in the following way

$$\pi_n = \frac{dP_n(\mu)}{d\mu}, \qquad \text{Eq. (1.5)}$$

$$\tau_n = \mu\pi_n(\mu) - (1-\mu^2)\frac{d\pi_n(\mu)}{d\mu}.$$

In addition to the angle-dependent functions, the Lorenz-Mie coefficients (a_n and b_n) are evaluated using the spherical Bessel functions

$$\psi_n(z) = z j_n(z), \qquad \text{Eq. (1.6)}$$

$$\zeta_n(z) = z\big(j_n(z) - i y_n(z)\big).$$

Using the spherical functions and their derivatives (denoted with primes), the complex-valued Lorenz-Mie coefficients are expressed as

$$a_n = \frac{\eta_{med}\, \psi_n'(y)\, \psi_n(x) - \eta\, \psi_n(y)\, \psi_n'(x)}{\eta_{med}\, \psi_n'(y)\, \zeta_n(x) - \eta\, \psi_n(y)\, \zeta_n'(x)}\,, \qquad \text{Eq. (1.7)}$$

$$b_n = \frac{\eta\, \psi_n'(y)\, \psi_n(x) - \eta_{med}\, \psi_n(y)\, \psi_n'(x)}{\eta\, \psi_n'(y)\, \zeta_n(x) - \eta_{med}\, \psi_n(y)\, \zeta_n'(x)}.$$

Here is η the refractive index of the particle, r is the particle radius, and x and y are size parameters which are expressed as: $x = 2\pi r \eta_{med}/\lambda$ and $y = 2\pi r \eta/\lambda$. Both a_n and b_n are infinite converging series and may be terminated once the error is at an acceptable level. The number of elements, M, to reach an acceptable level may be found using the following expression with p = 4.3,

$$M = \left\lceil |x| + p|x|^{1/3} + 1 \right\rceil. \qquad \text{Eq. (1.8)}$$

By applying eq. 1.8 with the specific value of p, the maximum error is 10^{-8} **[4–6]**. Thus, this provides an implementable expression for evaluating the scattered electric field. The abovementioned expression for the scattered electric field is only given for a single plane, and thus expanding this to any given point observed on an arbitrary sphere are expressed as

$$E_{s\theta} \sim E_0 \frac{e^{ikr}}{-ikr} \cos(\phi)\; S_2(\cos(\theta))\,, \qquad \text{Eq. (1.9)}$$

$$E_{s\phi} \sim -E_0 \frac{e^{ikr}}{-ikr} \sin(\phi)\; S_1(\cos(\theta))\,.$$

With these expressions we may calculate the scattered electric field in any direction and resolve it in the two orthogonal components.

1.2 Scattering by a homogeneous sphere situated in an inhomogeneous electric field

To accurately describe the scattered electric field from a single particle positioned in an interference pattern created by two or more incident monochromatic plane waves, we need to correctly sum each contribution of the scattered electric field produced by the total incident field. From Bohren and Huffman we know that superposition applies if each field contribution is a solution to Maxwell's equations (p. 60-61) **[3]**. In this case we solely investigate the scattered electric field from an interference pattern generated by two intersecting plane waves. The reference geometry of this is shown in **Supplementary Figure 1.2**.

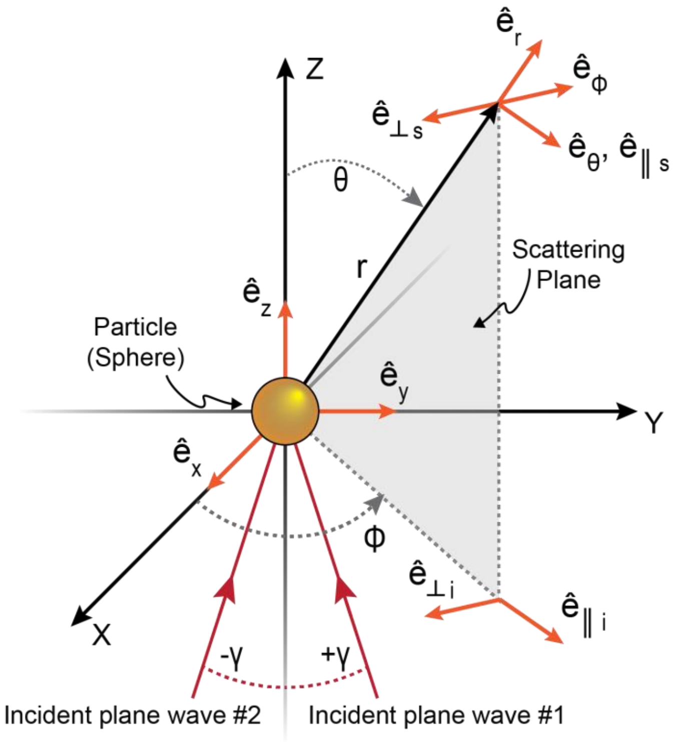

Supplementary Figure 1.2: Scattering from a spherical particle illuminated by two monochromatic plane waves. The incident waves propagate along the red trajectories within the YZ-plane and are oriented at angles of ±γ relative to the z-axis. The spherical particle is located at the origin of the coordinate system.

In this case both incident waves are symmetrically rotated by ±γ relative to the z-axis, meaning the incident fields are expressed as **[7]**

$$\mathbf{E}_{inc}^{(1)} = E_0 \, e^{ik(z\cos(\gamma)+y\sin(\gamma))} \, e^{i\varphi_1}, \qquad \text{Eq. (1.10)}$$

$$\mathbf{E}_{inc}^{(2)} = E_0 \, e^{ik(z\cos(\gamma)-y\sin(\gamma))} \, e^{i\varphi_2}.$$

An important aspect of the abovementioned expressions is the phase term $e^{i\varphi}$ ($e^{i\varphi_k}$) ($k = 1,2$), as this term is used to describe the relative position of the particle relative to the interference pattern. When both beams are polarized parallel to the x-axis, the interference pattern fringes will be parallel to the z-axis for all $\pi/2 \geq |\gamma| > 0$. Using the expressions from **Supplementary Section 1.1** to describe the scattered electric field generated from each beam, the resulting scattered field are expressed as the superposition of each scattered field rotated accordingly to the incident beams **[8]**

$$\mathbf{E}_{sca} = e^{i\varphi_1} \, \mathbf{E}_{sca}^{(1)} + e^{i\varphi_2} \, \mathbf{E}_{sca}^{(2)}. \qquad \text{Eq. (1.11)}$$

Here, $\mathbf{E}_{sca}^{(1)}$ and $\mathbf{E}_{sca}^{(2)}$ represent the scattered electric field contribution from each incident beam. From this expression describing the total scattered electric field, the total scattered intensity of this is expressed as

$$\mathbf{I}_{sca} = \left|\mathbf{E}_{sca}^{(1)}\right|^2 + \left|\mathbf{E}_{sca}^{(2)}\right|^2 + 2\,\mathrm{Re}\left(e^{i\varphi_{int}} \, \mathbf{E}_{sca}^{(1)} \, \mathbf{E}_{sca}^{(2)\,*}\right). \qquad \text{Eq. (1.12)}$$

Here the asterisk represents the complex conjugate, while the phase term $e^{i\varphi_{int}}$ for the interference pattern controls the oscillating behaviour of the total incident electric field. The phase term may be written in diverse ways depending on if the particle is moving within a stationary interference pattern or vice versa. In the case of a moving particle within a stationary interference pattern the phase term will be $e^{ik_f Y}$, where $k_f = 2\pi/\lambda_f$ is the wavenumber for interference pattern, and $\lambda_f = \lambda/\sin(\gamma)$ is the interference wavelength **[7]**. However, if the particle is stationary in a scrolling interference pattern the phase term may be written as $e^{i(\varphi_1-\varphi_2)}$ describing the phase difference between the two incident beams. Using the expression in **eq. 1.12** we can describe the intensity of the scattered electric field from a single particle positioned in an interference pattern.

1.3 Scattering by small particles from every perspective using spherical partitioning

To effectively evaluate the scattered electric field in every direction we use a spherical partitioning algorithm to discretize the continuous functions describing the scattered intensity in every angle possible. For this work, we outline a set of criteria to evaluate spherical partitioning function. First, the sampling points should be uniformly distributed across the spherical surface. Second, the total surface area must remain consistent across different partitioning schemes, with each partition representing an equal fraction of the surface. Third, the method should allow straightforward adjustment of point density or resolution. A naïve approach for distributing points on a sphere using a linear distribution of $\phi = [0, 2\pi]$ and $\theta = [0, \pi]$ is illustrated in **Supplementary Figure 1.3a**.

Several existing approaches satisfy these criteria to varying degrees **[9–12]** . We find that the method proposed by Holhoş et al. meets the requirements effectively **[12]**. In this approach, the sphere is divided into eight regions corresponding to the faces of an octahedron, as illustrated in **Supplementary Figure 1.3b**. Each face can be recursively subdivided into smaller triangular elements according to a defined mathematical rule. The number of subdivisions n determines the total number of points on the sphere: the number of triangle vertices is given by $M = 4n^2+2$, and the number of triangle centers is $M = 8n^2$, yielding a total of $M = 12n^2+2$ sampling points.

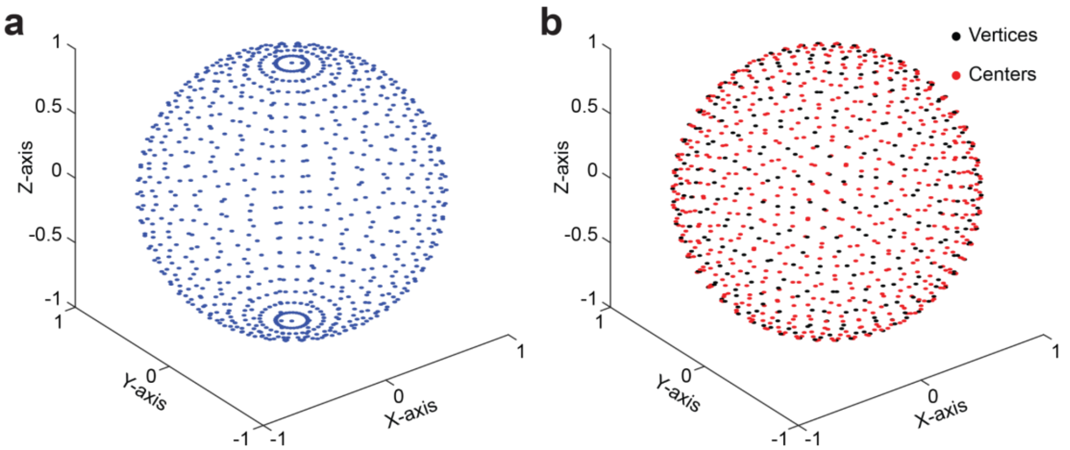

Supplementary Figure 1.3: (a) Point distribution using a naïve linear sampling of both θ and ϕ. Total number of points: *M=872*. **(b)** Spherical sampling based on an octahedral partitioning scheme, generating an area-preserving triangular grid. Triangle vertices for subdivision level *n=9* are shown in black, and triangle centers in red. Total number of points: *M=974*.

1.4 Rotation in spherical coordinates using an orthonormal basis

To practically implement the contribution from each beam to the total scattered field, we need to rotate the evaluated scattered field in every point on the discretized unit sphere. Quaternions provide an efficient framework for performing arbitrary three-dimensional rotations of vectors. Frisvad has shown that it is possible to construct an orthonormal basis that enables free rotation of a given unit vector around a selected rotation axis using quaternion operations **[13]**. The method is designed for graphics-oriented applications and therefore minimizes computational cost.

This approach permits efficient rotation of the z-axis to an arbitrary direction on the unit sphere while simultaneously generating an orthonormal basis aligned with the new orientation, as illustrated in **Supplementary Figure 1.4**. In this context, the unit vector corresponding to the z-axis, $\vec{z} = (0, 0, 1)$, representing the surface normal in the local space, is rotated to a new surface normal $\vec{n} = (n_x, n_y, n_z)$ in the global space. The rotation of any unit vector $\overrightarrow{\perp \omega} = (x, y, z)$ from the local space into the global space, $\vec{\omega}$, is then obtained using the following expression **[13,14]**:

$$\vec{\omega} = \left(x \begin{bmatrix} 1 - n_x^2/(1+n_z) \\ -n_x\, n_y/(1+n_z) \\ -n_x \end{bmatrix} + y \begin{bmatrix} -n_x\, n_y/(1+n_z) \\ 1 - n_y^2/(1+n_z) \\ -n_y \end{bmatrix} + z \begin{bmatrix} n_x \\ n_y \\ n_z \end{bmatrix} \right). \qquad \text{Eq. (1.13)}$$

A singularity occurs in the expression when $1+n_z = 0$, corresponding to the south pole of the unit sphere. This issue is addressed by applying an optimal threshold ($n_z < 0.9999805689$) and, in such cases, setting $\vec{\omega} = (-x,-y,-z)$. Alternatively, the singularity can be relocated from the south pole to the equator **[15]**.

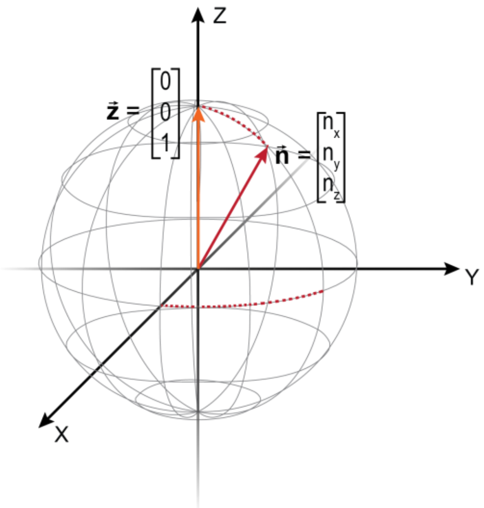

Supplementary Figure 1.4: Rotation of the z-axis, $\vec{z} = (0, 0, 1)$, to a new arbitrary direction on a unit sphere denoted as $\vec{n} = (n_x, n_y, n_z)$.

To facilitate vector rotation, we construct a rotation matrix from an orthonormal basis. This enables the use of standard matrix multiplication to rotate any unit vector from the local space to the global space. The same procedure applies when using the transpose of the rotation matrix, allowing rotation from the global space back to the local space.

$$\text{Local} \rightarrow \text{Global:} \quad \begin{bmatrix} x_g \\ y_g \\ z_g \end{bmatrix} = \mathbf{R} \begin{bmatrix} x_l \\ y_l \\ z_l \end{bmatrix}, \qquad \text{Eq. (1.14)}$$

$$\text{Global} \rightarrow \text{Local:} \quad \begin{bmatrix} x_l \\ y_l \\ z_l \end{bmatrix} = \mathbf{R}^T \begin{bmatrix} x_g \\ y_g \\ z_g \end{bmatrix},$$

$$\mathbf{R} = \begin{bmatrix} 1 - n_x^2/(1+n_z) & -n_x\, n_y/(1+n_z) & n_x \\ -n_x\, n_y/(1+n_z) & 1 - n_y^2/(1+n_z) & n_y \\ -n_x & -n_y & n_z \end{bmatrix}.$$

1.6 Mie simulations

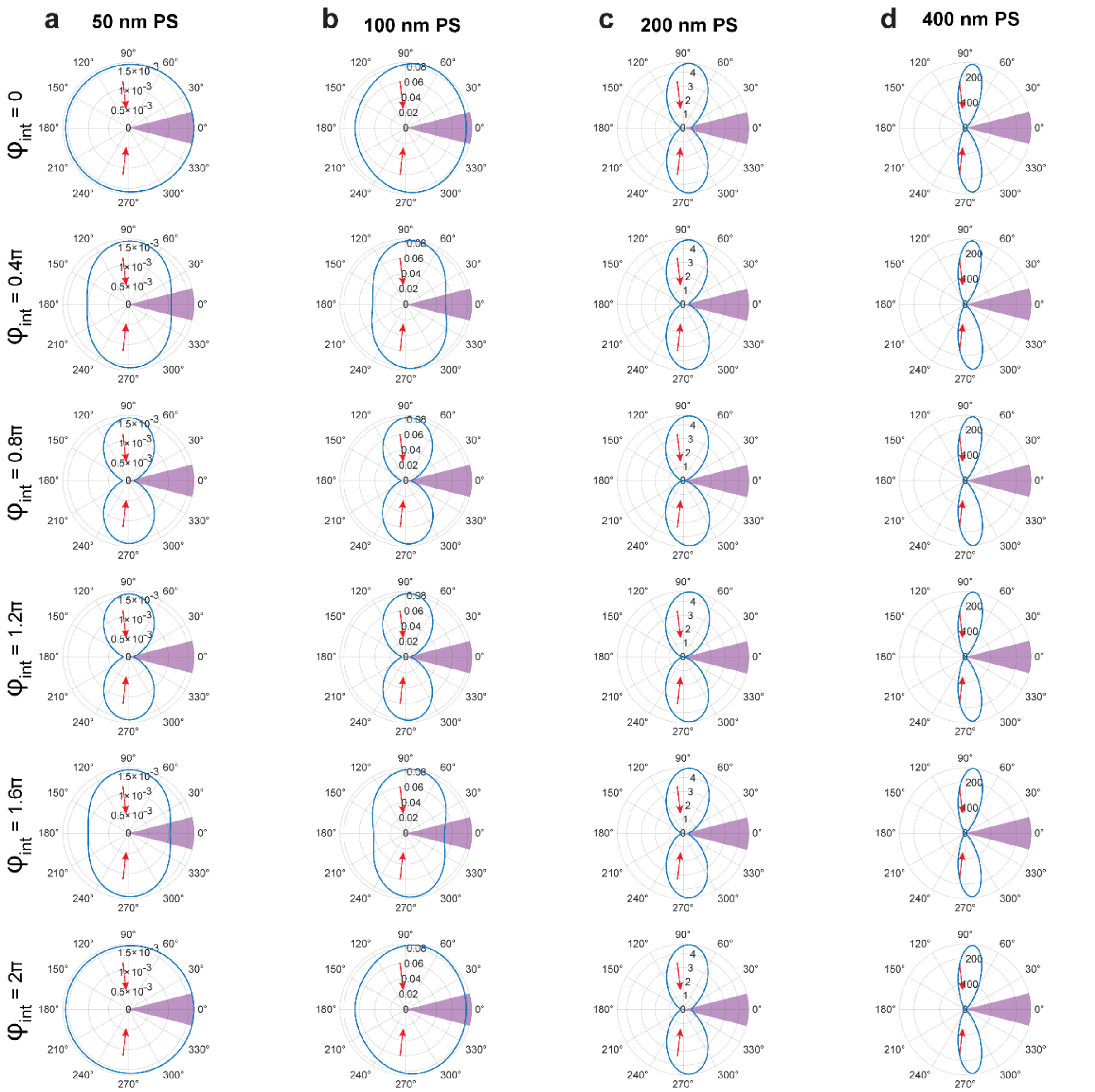

Supplementary Figure 1.6: Scattering cross sections for gold nanoparticles of varying sizes (n_p=1.6833+1.8849i) illuminated by an inhomogeneous light field. Two nearly counter-propagating beams (*γ=83°*), indicated by red arrows, with wavelength λ=355 nm, propagate through a homogeneous water medium (n_{med}=1.3426) and generate a scrolling interference pattern. The blue outline shows the scattering intensity in the indicated direction for each cross section. The relative phase of the interference pattern is shown on the left for each particle size. Four particle diameters are simulated: **(a)** 50 nm Au, **(b)** 100 nm Au, **(c)** 200 nm Au, and **(d)** 400 nm Au.

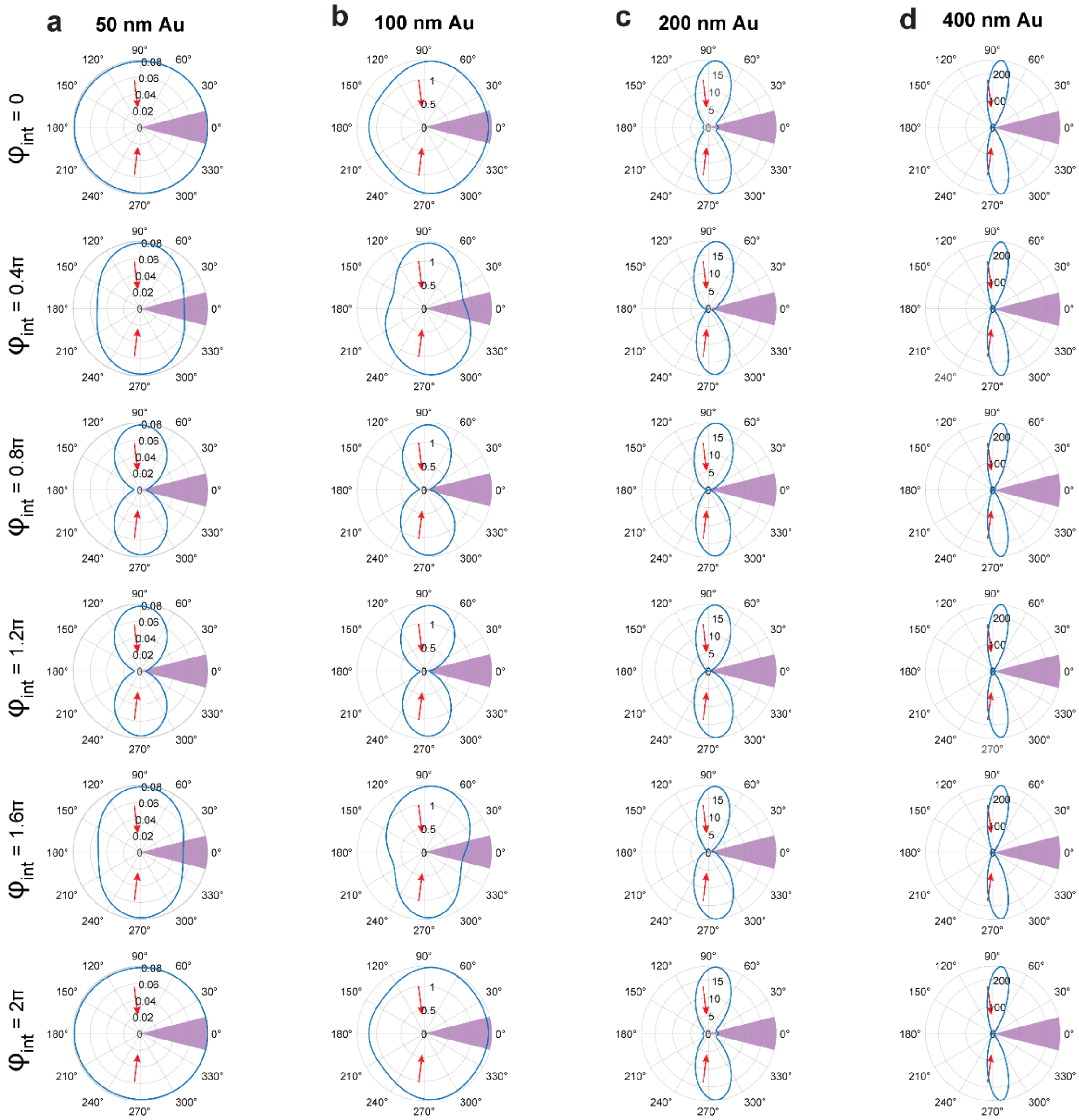

Supplementary Figure 1.7: Scattering cross sections for polystyrene nanoparticles of varying sizes (n_p=1.636 + 0.008i) illuminated by an inhomogeneous light field. Two nearly counter-propagating beams (γ=*83°*), indicated by red arrows, with wavelength λ=355 nm, propagate through a homogeneous water medium (n_{med}=1.3426) and generate a scrolling interference pattern. The blue outline shows the scattering intensity in the indicated direction for each cross section. The relative phase of the interference pattern is shown on the left for each particle size. Four particle diameters are simulated: **(a)** 50 nm PS, **(b)** 100 nm PS, **(c)** 200 nm PS, and **(d)** 400 nm PS.

2. Materials and methods

2.1 Signal Generation

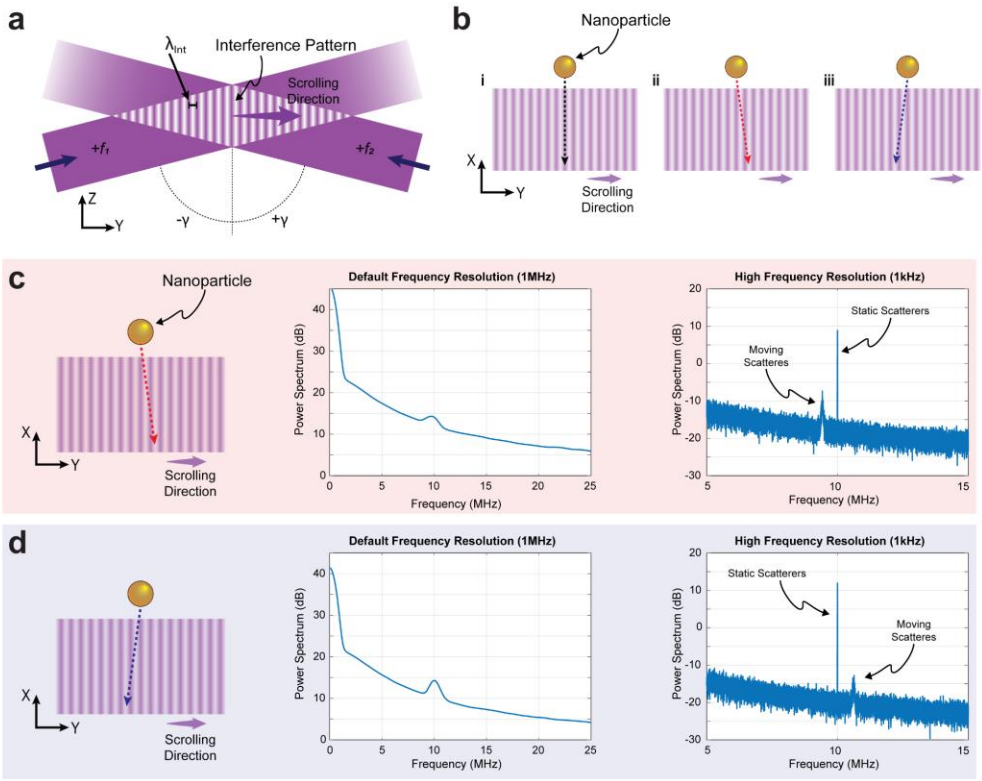

Supplementary Figure 2.1: (a) Two frequency-shifted, nearly collinear beams form a scrolling interference pattern; its wavelength is determined by the incident wavelength and the angle between the beams. **(b)** Three example particle trajectories: motion parallel to the fringes produces no frequency shift, while angled trajectories generate red- or blue-shifted intensity oscillations due to Doppler effects. **(c)** Particles with a small velocity component parallel to the scrolling direction exhibit a red-shifted scattered signal, as seen in the power spectrum compared with static scatterers. **(d)** Particles with a velocity component antiparallel to the scrolling motion exhibit a corresponding blue shift.

2.2 Data Processing

2.2.1 Threshold value

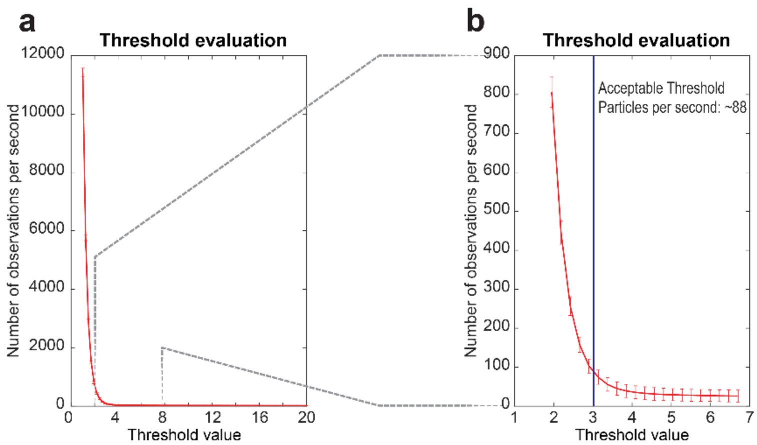

Supplementary Figure 2.2: **(a)** Number of detections in a blank ultrapure H_2O sample as a function of the applied threshold. **(b)** Zoom-in the threshold range 2–7. The vertical blue line marks the selected threshold of 3, yielding approximately 88 detections per second.

2.2.2 Data processing flow chart (dual beam)

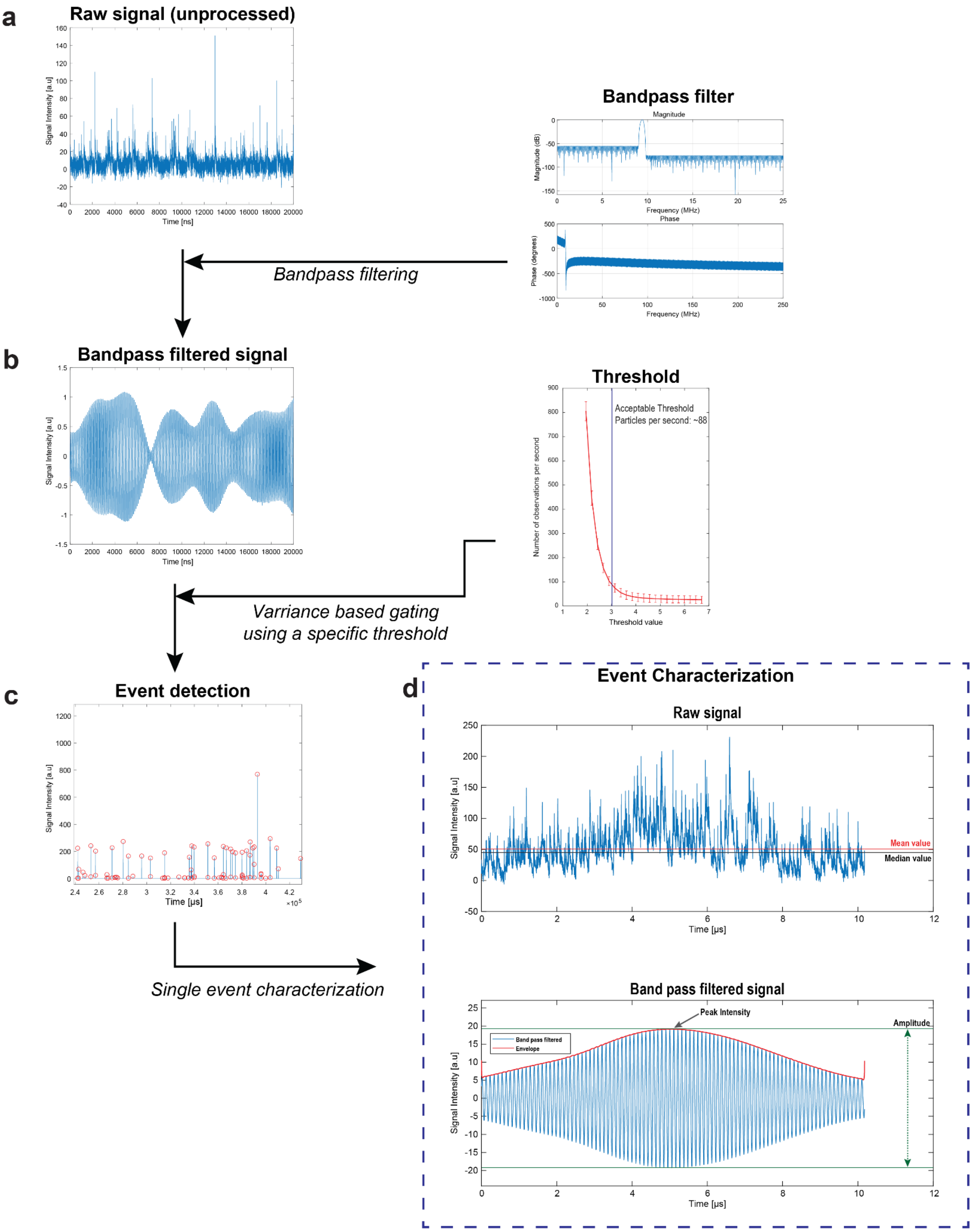

Supplementary Figure 2.3: Data process flow for dual-beam configuration, from receiving the unprocessed data stream from the FPGA to identifying and characterizing single events. **(a)** Unprocessed data streamed from the FPGA to the host computer. **(b)** Applying a FIR bandpass filter to reject background noise and isolate signal elicited from traversing particles. **(c)** Variance based gating of bandpass filtered signal sections of 1 μs duration for identifying single events. **(d)** Single event characterization by extraction signal properties using both raw and filtered signals.

2.2.3 Data processing flow chart (single beam)

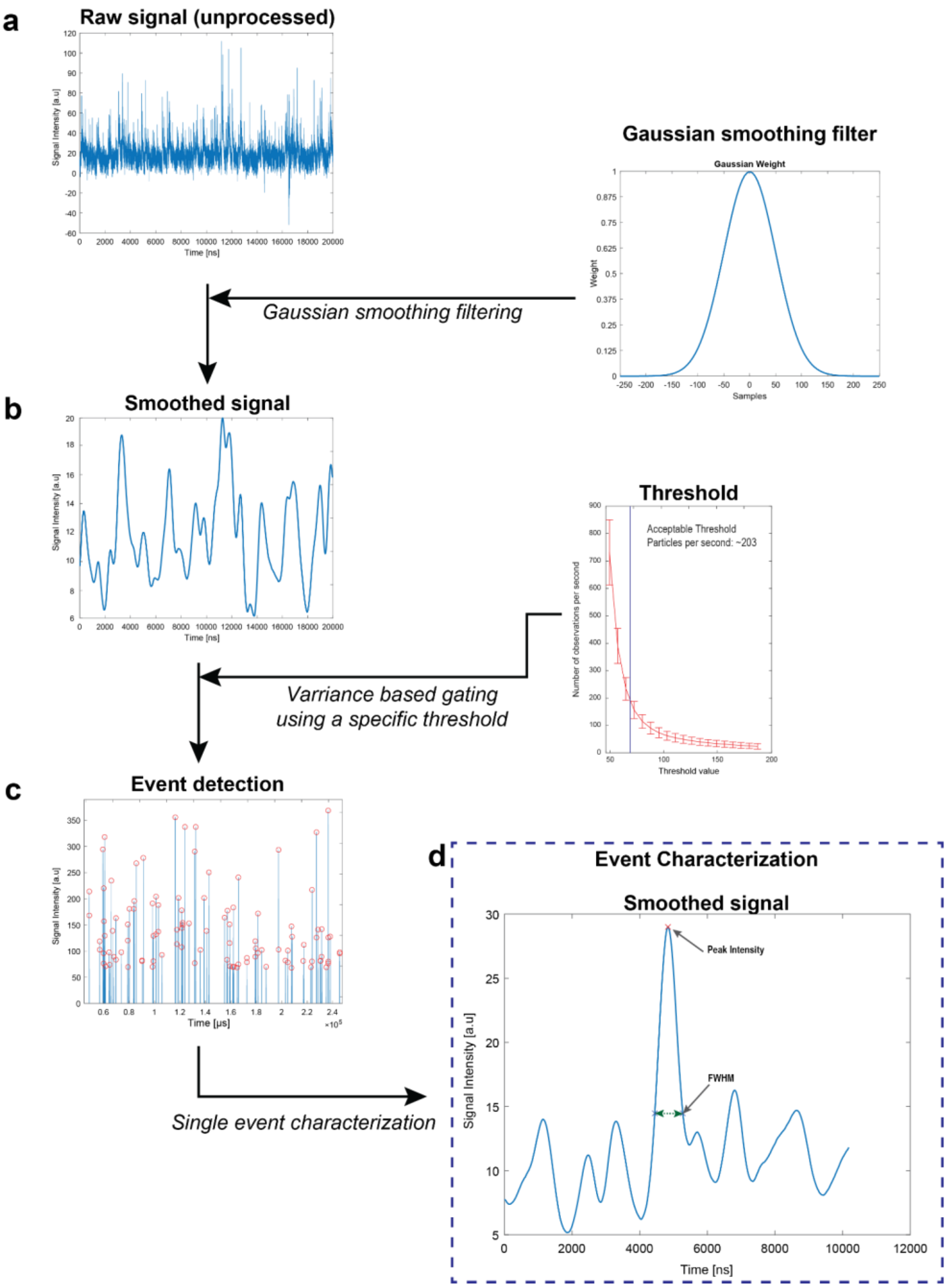

Supplementary Figure 2.4: Data process flow for single-beam configuration, from receiving the unprocessed data stream from the FPGA to identifying and characterizing single events. **(a)** Unprocessed data streamed from the FPGA to the host computer. **(b)** Applying a Gaussian running average filter to smooth the signal received from the FPGA. **(c)** Variance based gating of bandpass filtered signal sections of 1 μs duration for identifying single events. **(d)** Single event characterization by extraction signal properties using the smoothed signal.

2.2.4 Flow characterization

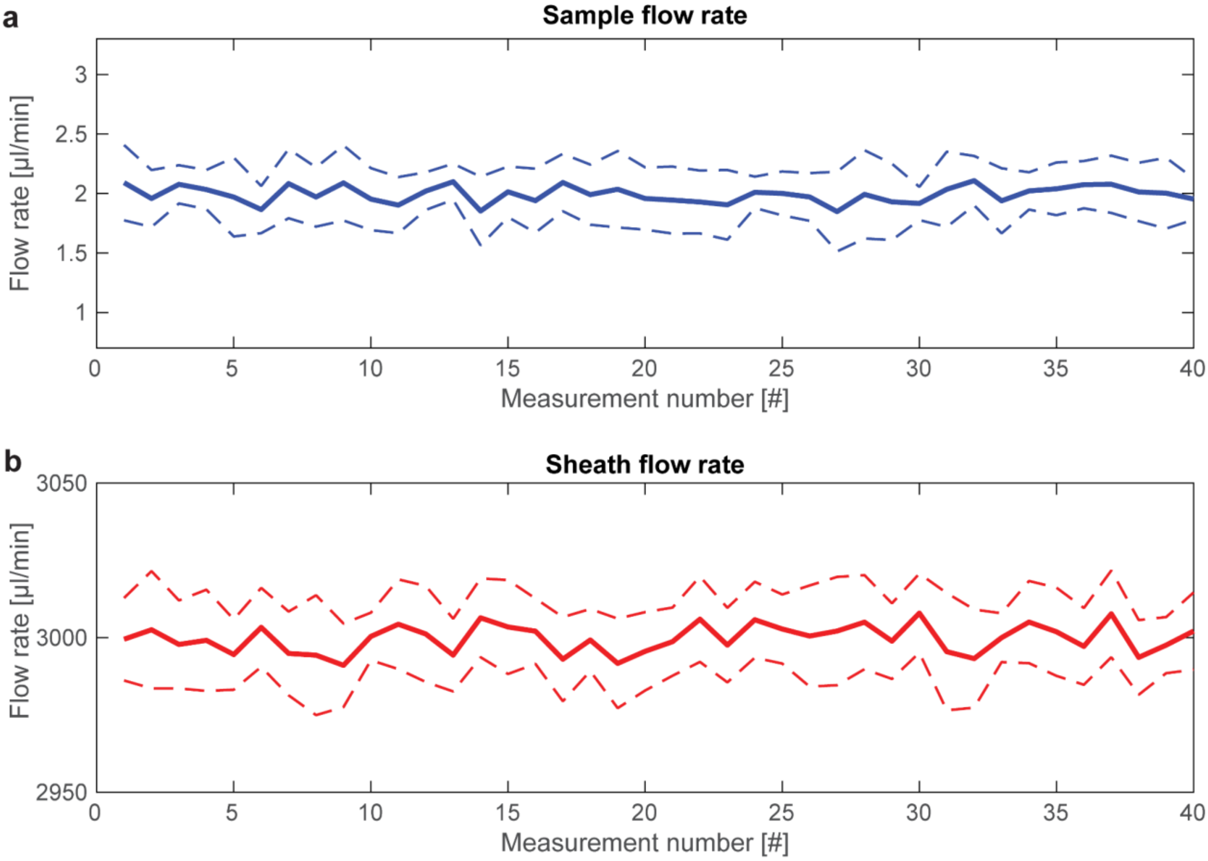

Supplementary Figure 2.5: Characterization of flow rate evaluated for each sample measurement (40 in total) for every particle population. **(a)** Characterization of sample flow rate for every particle population. The mean sample flow rate is shown with a solid blue line, and the dashed blue lines indicate ± one standard deviation. **(b)** Characterization of sheath flow rate for every particle population. The mean sheath flow rate is shown with a solid red line, and the dashed red lines indicate ± one standard deviation.

3. Supplementary Data

3.1 Flow Cytometry controls

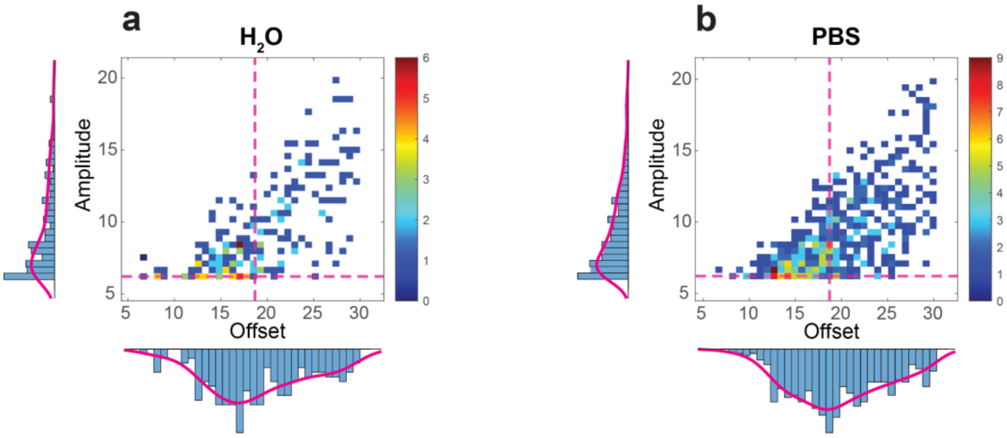

Supplementary Figure 3.1: Each panel displays event distributions based on signal offset and amplitude. Heatmaps with corresponding color bars indicate observation frequency, while marginal histograms show the distribution of each parameter. A magenta kernel outlines the marginal distribution, and dashed lines marking the respective peaks of the specific distribution. Blank measurements of **(a)** Ultra purified water and **(b)** Phosphate-Buffered Saline (PBS).

3.2 Signal Histogram

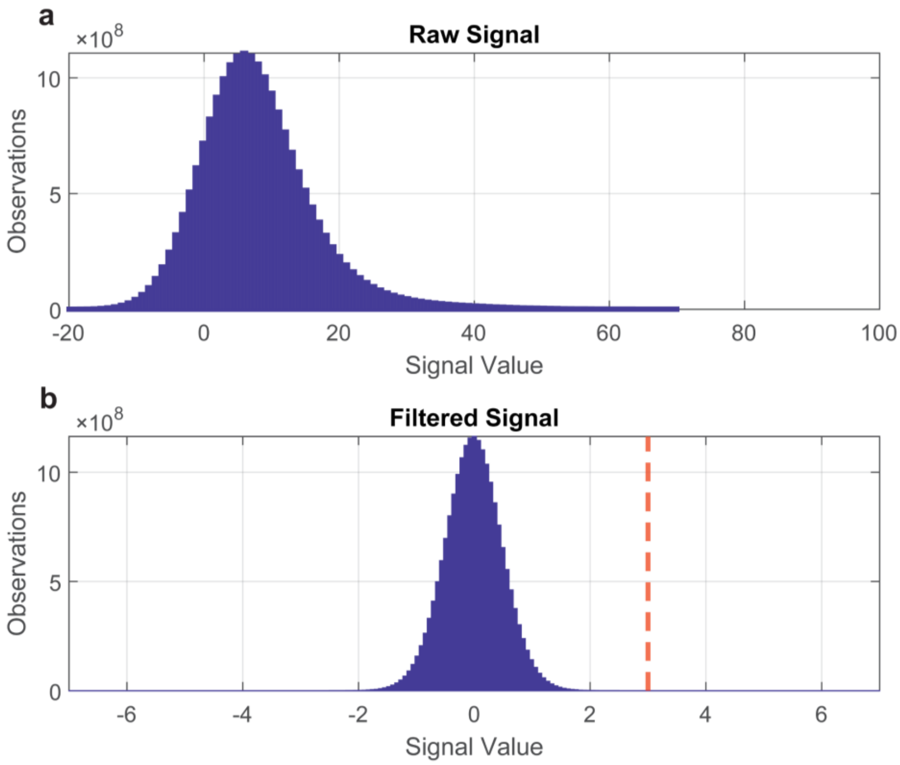

Supplementary Figure 3.2: Comparison of signal histograms for the unfiltered signal **(a)** and the bandpass-filtered signal **(b)**. In each histogram, the horizontal axis denotes the signal value bins, while the vertical axis represents the corresponding number of observations. The red vertical line indicates the threshold gating value applied to the bandpass-filtered signal.

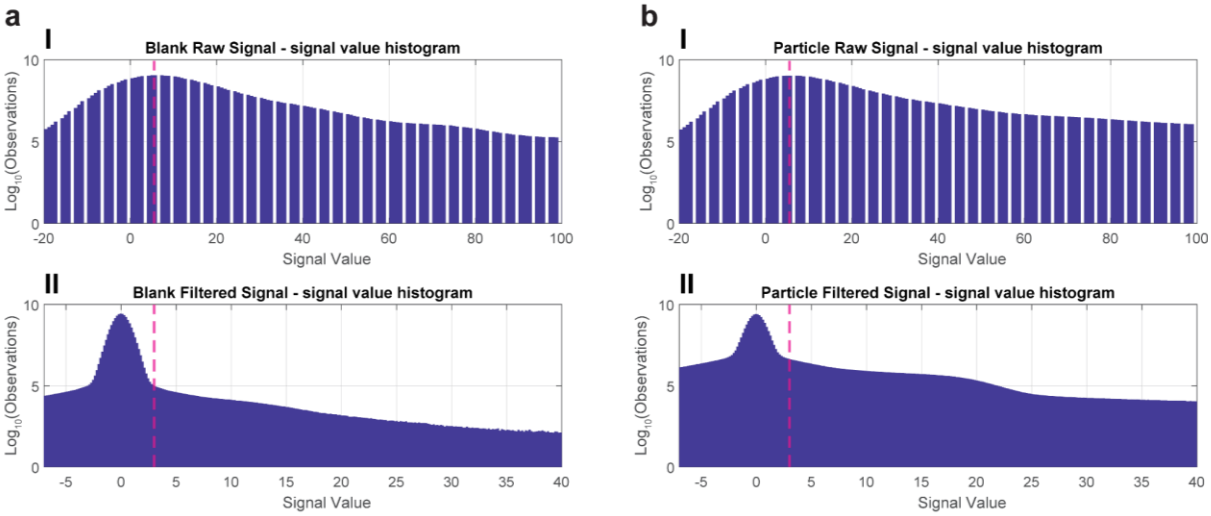

Supplementary Figure 3.3: Comparison of signal histograms for blank sample **(a)** and for a sample containing 125 nm Au particles **(b)**. For each sample two histograms are provided; the horizontal axis denotes the signal value bins, and the vertical axis represents the $\log_{10}$ transformed number of observations. Panel (I) displays the histogram of the unfiltered signal for both the blank and particle samples, whereas panel (II) shows the histogram of the bandpass-filtered signals. The magenta vertical lines indicate the threshold gating value applied to the bandpass-filtered signals.

3.3 DLS Measurements

Listed size (nm)	Z-average	Intensity mean	Polydispersity index
Gold particles (Au)			
15 nm	NaN	NaN	NaN
30 nm	40.6 ± 7.2 nm	144.9 ± 81.8 nm	0.312 ± 0.127
50 nm	64.9 ± 1.2 nm	79.5 ± 1.7 nm	0.179 ± 0.007
70 nm	81.5 ± 0.34 nm	88.6 ± 5.2nm	0.149 ± 0.010
125 nm	129.0 ± 0.8 nm	136.3 ± 5.2 nm	0.101 ± 0.018
150 nm	154.7 ± 2.7 nm	158.0 ± 3.3 nm	0.114 ± 0.076
200 nm	262.0 ± 6.4 nm	258.9 ± 4.0 nm	0.123 ± 0.127
500 nm	783.5 ± 33.1 nm	485.4 ± 46.1 nm	0.522 ± 0.055
Polystyrene (PS)			
100 nm	126.3 ± 0.6 nm	134.7 ± 1.1 nm	0.070 ± 0.012
152 nm	164.4 ± 1.4 nm	171.5 ± 1.0 nm	0.025 ± 0.008
200 nm	212.8 ± 1.5 nm	221.4 ± 1.5 nm	0.009 ± 0.007
300 nm	364.0 ± 15.1 nm	337.1 ± 22.6 nm	0.344 ± 0.250
400 nm	424.5 ± 1.2 nm	443.1 ± 2.7 nm	0.048 ± 0.034
495 nm	538.3 ± 1.3 nm	577.5 ± 9.7 nm	0.103 ± 0.046

3.4 Dilution Experiments

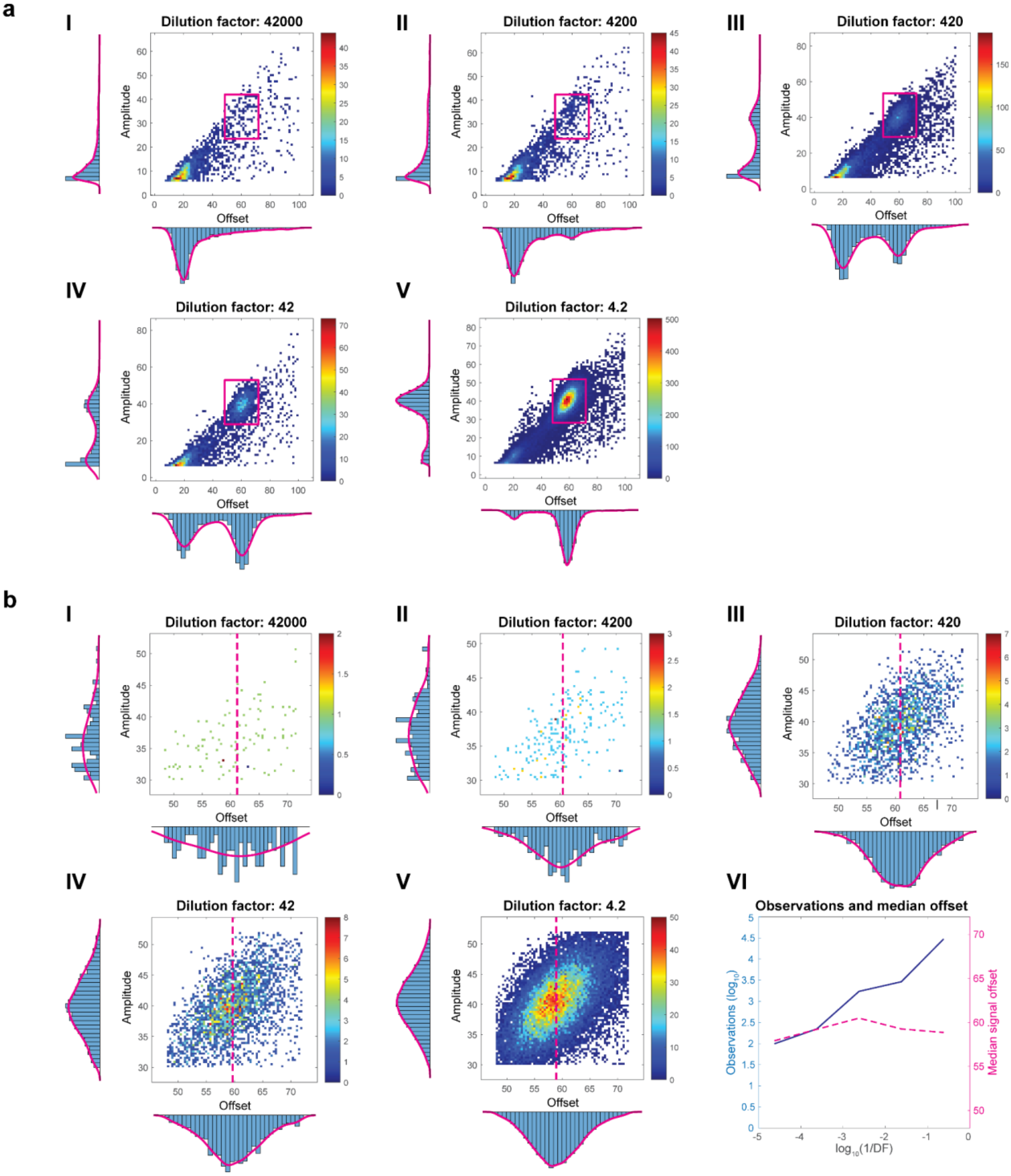

Supplementary Figure 3.4: Serial dilution experiment with 125 nm Au particles, in steps of 10-fold dilution concentration steps. Each panel displays event distributions based on signal offset and amplitude. Heatmaps with corresponding color bars indicate observation frequency, while marginal histograms show the distribution of each parameter. **(a)** Shows the total number of events for each dilution factor shown in panel I-V. A magenta colored box outlines the region of where particles are expected to appear within. **(b)** Displays a zoomed in view of each magenta box, providing a finer resolution of the event distribution. A vertical line indicates the median of the signal offset for every panel from I-V. Panel VI shows the total number of observed events (solid blue line) and the median signal offset (dashed magenta line) in panel I-V as a function of the $\log_{10}$ reciprocal dilution factor.

3.5 Histogram signal offset

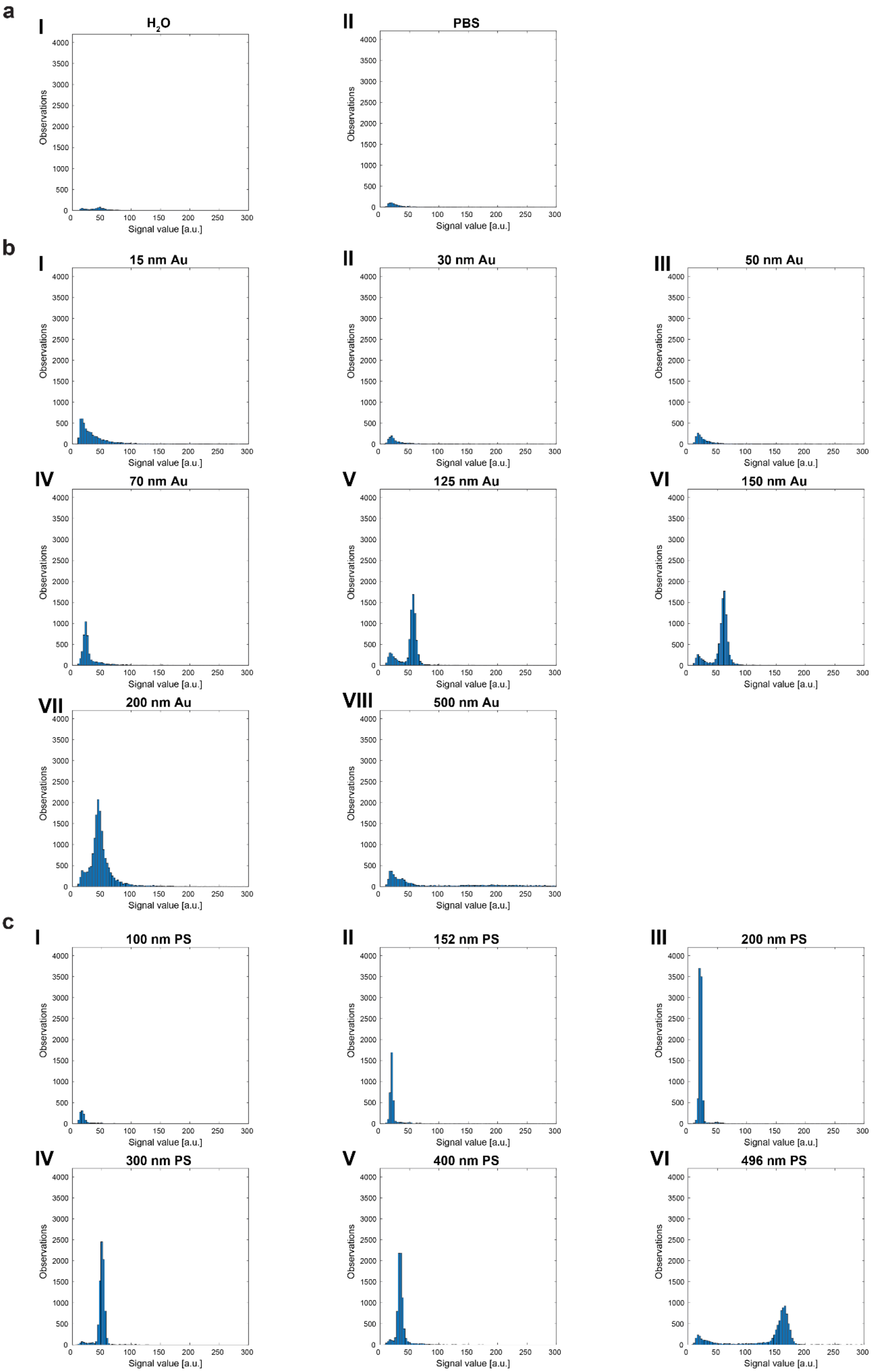

Supplementary Figure 3.5: Signal offset is shown for every detected event using the dual-beam configuration. Original 2D heatmap data for each panel is provided in Supplementary Figure 3.1 and Main Figure 2. Each panel displays the distribution of signal offsets using shared axes, where the horizontal axis represents the offset and the vertical axis shows the number of observations. **(a)** Shows the distribution of events for a blank sample and a PBS sample, **(b)** shows the distribution of events for Au particles, and **(c)** shows the distribution of events for PS particles.

4. MIFlowCyt compliant item check list

The following table described the minimum information required about the conducted flow cytometry experiments within this work, according to the MIFlowCyt standard **[16]**.

1. Experiment overview	
1.1 Purpose	The aim of this study was to investigate to which extent using a scrolling interference pattern for illuminating submicron sized particles in a flow, could improve the ability to characterize and differentiate various particle populations based on size and refractive index. Specifically, this study focused on light scattering based characterization of spherical particle populations of gold and polystyrene varying in size from 15 nm to 500 nm. The overall goal of this work was to demonstrate the effect of using an interference pattern that continuously scrolls across the interrogation zone, can encode spatial information in the illumination, and by frequency lock-in of the scattered light signals reject broadband noise.
1.2 Keywords	Flow Cytometry; Interference pattern; Submicron particles; label-free; Acousto optic frequency shifters; Frequency lock-in; High-throughput; Lorenz-Mie
1.3 Experiment variables	Particle population; particle size; index of refraction;
1.4 Organization name and address	Department of Health Technology Ørsteds Plads, Building 345C DK-2800 Kgs. Lyngby Denmark
1.5 Primary contact name and email address	Carl Emil Schøier Kovsted (cesk@dtu.dk) Emil Boye Kromann (ebbk@igt.sdu.dk)
1.6 Date or time of experiment	September 2025 - December 2025
1.7 Conclusions	This work presents a label-free FCM platform for submicron particle characterization using scrolling interference pattern illumination. Based on high-throughput measurements of well-defined spherical particles, we demonstrate detection limits down to 15 nm for Au and 100 nm for PS at rates up to 750 particles/s. The observed scattering intensities align with Lorenz-Mie predictions for inhomogeneous light fields. In summary, this method offers a high-

	throughput, high-sensitivity, and label-free solution for submicron particle analysis.
1.8 Quality control measures	Daily quality control measures: *Cleaning fluidics system:* The sample loop is daily loaded and flushed with 5% Triton-X (Sigma-Aldrich, X100RS), and excess detergent fluid is flushed to a waste container. The sample flow rate is 80 µL/min. After 4 minutes of flushing, the flow cell is flushed with MiliQ-water - to remove excess detergent inside the tubing. This procedure serves to remove particles that adhere to any side walls of the flow cell or on the interior of the tubes. Sample-specific controls: Blank controls (including ultrapure water and buffer): see Supplementary Figure 3.1, Supplementary Figure 3.3, Supplementary Figure 3.5) Gold particle samples: see Supplementary Figure 3.3, Supplementary Figure 3.4, Supplementary Figure 3.5 Polystyrene particle samples: see Supplementary Figure 3.5 Flow rate control measures: See Supplementary Figure 2.5
2. Flow Sample (specimen)	
2.1 Material and source	Refer to methods subsection "*Materials (beads & buffers)*"
2.2 Treatments	Prior to all measurements, the particles diluted in MiliQ water were treated in an ultrasonic bath for 5-10 minutes to prevent particle aggregates.
2.3 Reagents	Refer to methods subsection "*Materials (beads & buffers)*" *Triton-X (Sigma-Aldrich, X100RS)*
Instrument details	
3.1 Instrument name	Custom flow cytometer
3.2 Optical path	Refer to methods subsection "*Flow cytometer set-up*" and *"Optical Setup"*
3.3 Fluidics	Refer to methods subsection "*Flow cytometer set-up*" and *"Fluidics Setup"*
3.4 Instrument electronics	Refer to methods subsection "*Flow cytometer set-up*" and *"Electronics Setup"*
4. Data analysis	

4.1 Gate description	Refer to methods subsection "*Flow cytometry analysis"*, and Supplementary Figure 3.2, Supplementary Figure 3.3 and Supplementary Figure 3.4 Supplementary Figure 2.2 depicts the gating was determined based on events per second detected.
4.2 Event detection and characterization	Refer to results subsection "*Operation of the flow cytometer"*, Supplementary Figure 2.3 and Supplementary Figure 2.4
4.3 Lower detection limit	Refer to results subsection "*Lower detection limit in dual-beam operation compared to single-beam operation",* and supplementary Figure 3.4
4.4 Analysis software	Analysis was performed in MATLAB (MathWorks, MATLAB R2022B) with custom written scripts. Scripts can be acquired by e-mail.

5. References

1. L. Lorenz, "Light propagation in and outside a sphere illuminated by plane waves of light," The European Physical Journal H **44**, 77–135 (2019).

2. G. Mie, "Beiträge zur Optik trüber Medien, speziell kolloidaler Metallösungen," Ann. Phys. **330**, 377–445 (1908).

3. C. F. Bohren and D. R. Huffman, *Absorption and Scattering of Light by Small Particles* (Wiley, 1998).

4. J. R. Frisvad, N. J. Christensen, and H. W. Jensen, "Computing the scattering properties of participating media using Lorenz-Mie theory," ACM Trans. Graph. **26**, 60 (2007).

5. W. J. Wiscombe, "Improved Mie scattering algorithms," Appl. Opt. **19**, 1505 (1980).

6. V. E. Cachorro and L. L. Salcedo, "New Improvements for Mie Scattering Calculations," J. Electromagn. Waves Appl. **5**, 913–926 (1991).

7. A. R. Jones, "Light scattering by a sphere situated in an interference pattern, with relevance to fringe anemometry and particle sizing," J. Phys. D Appl. Phys. **7**, 310 (1974).

8. C R Negus and L E Drain, "Mie calculations of the scattered light from a spherical particle traversing a fringe pattern produced by two intersecting laser beams," J. Phys. D Appl. Phys. **15**, 375–402 (1982).

9. R. G. Gibb, "The rHEALPix Discrete Global Grid System," IOP Conf. Ser. Earth Environ. Sci. **34**, 012012 (2016).

10. R. Sadourny, A. Arakawa, and Y. Mintz, "Integration of the divergent barotropic vorticity equation with an icosahedral-hexagonal grid for the sphere," Mon. Weather Rev. **96**, 351–356 (1968).

11. E. L. Altschuler, T. J. Williams, E. R. Ratner, R. Tipton, R. Stong, F. Dowla, and F. Wooten, "Possible Global Minimum Lattice Configurations for Thomson's Problem of Charges on a Sphere," Phys. Rev. Lett. **78**, 2681–2685 (1997).

12. A. Holhoş and D. Roşca, "An octahedral equal area partition of the sphere and near optimal configurations of points," Computers & Mathematics with Applications **67**, 1092–1107 (2014).

13. J. R. Frisvad, "Building an Orthonormal Basis from a 3D Unit Vector Without Normalization," Journal of Graphics Tools **16**, 151–159 (2012).

14. N. Max, "Improved accuracy when building an orthonormal basis," Journal of Computer Graphics Techniques (JCGT) **6**, 9–16 (2017).

15. T. Duff, J. Burgess, P. Christensen, C. Hery, A. Kensler, M. Liani, and R. Villemin, "Building an Orthonormal Basis, Revisited," Journal of Computer Graphics Techniques (JCGT) **6**, 1–8 (2017).

16. J. A. Lee, J. Spidlen, K. Boyce, J. Cai, N. Crosbie, M. Dalphin, J. Furlong, M. Gasparetto, M. Goldberg, E. M. Goralczyk, B. Hyun, K. Jansen, T. Kollmann, M. Kong, R. Leif, S. McWeeney, T. D. Moloshok, W. Moore, G. Nolan, J. Nolan, J. Nikolich-Zugich, D. Parrish, B. Purcell, Y. Qian, B. Selvaraj, C. Smith, O. Tchuvatkina, A. Wertheimer, P. Wilkinson, C. Wilson, J. Wood, R. Zigon, R. H. Scheuermann, and R. R. Brinkman, "MIFlowCyt: The minimum information about a flow cytometry experiment," Cytometry Part A **73**, 926–930 (2008).